The Astrophysical Journal, 927:123 (15pp), 2022 March 1 https://doi.org/10.3847/1538-4357/ac4891

Detailed Chemical Abundances for a Benchmark Sample of M Dwarfs from the APOGEE Survey

Diogo Souto[1], Katia Cunha[2,3], Verne V. Smith[4], C. Allende Prieto[5,6], Kevin Covey[7], D. A. García-Hernández[5,6], Jon A. Holtzman[8], Henrik Jönsson[9], Suvrath Mahadevan[10,11], Steven R. Majewski[12], Thomas Masseron[5,6], Marc Pinsonneault[13], Donald P. Schneider[10], Matthew Shetrone[14], Keivan G. Stassun[15], Ryan Terrien[16], Olga Zamora[5,6], Guy S. Stringfellow[17], Richard R. Lane[18], Christian Nitschelm[19], and Bárbara Rojas-Ayala[20]
[1] Departamento de Física, Universidade Federal de Sergipe, Av. Marechal Rondon, S/N, 49000-000 São Cristóvão, SE, Brazil; diogosouto@academico.ufs.br
[2] Steward Observatory, University of Arizona, 933 North Cherry Avenue, Tucson, AZ 85721-0065, USA
[3] Observatório Nacional/MCTIC, R. Gen. José Cristino, 77, 20921-400, Rio de Janeiro, Brazil
[4] NOIRlab, 950 North Cherry Avenue, Tucson, AZ 85719, USA
[5] Instituto de Astrofísica de Canarias, E-38205 La Laguna, Tenerife, Spain
[6] Departamento de Astrofísica, Universidad de La Laguna, E-38206 La Laguna, Tenerife, Spain
[7] Department of Physics & Astronomy, Western Washington University, Bellingham, WA 98225, USA
[8] New Mexico State University, Las Cruces, NM 88003, USA
[9] Materials Science and Applied Mathematics, Malmö University, SE-205 06 Malmö, Sweden
[10] Department of Astronomy & Astrophysics, Pennsylvania State, 525 Davey Lab, University Park, PA 16802, USA
[11] Center for Exoplanets & Habitable Worlds, Pennsylvania State, 525 Davey Lab, University Park, PA 16802, USA
[12] Department of Astronomy, University of Virginia, Charlottesville, VA 22904-4325, USA
[13] Department of Astronomy, The Ohio State University, Columbus, OH 43210, USA
[14] University of Texas at Austin, McDonald Observatory, Fort Davis, TX 79734, USA
[15] Department of Physics and Astronomy, Vanderbilt University, 6301 Stevenson Center Ln., Nashville, TN 37235, USA
[16] Department of Physics & Astronomy, Carleton College, Northfield MN, 55057, USA
[17] Center for Astrophysics and Space Astronomy, University of Colorado, Campus Box 389, Boulder, CO 80309-0389, USA
[18] Centro de Investigación en Astronomía, Universidad Bernardo O'Higgins, Avenida Viel 1497, Santiago, Chile
[19] Centro de Astronomía (CITEVA), Universidad de Antofagasta, Avenida Angamos 601, Antofagasta 1270300, Chile
[20] Instituto de Alta Investigación, Universidad de Tarapacá, Casilla 7D, Arica, Chile
Received 2021 October 20; revised 2022 January 2; accepted 2022 January 3; published 2022 March 9

Abstract

Individual chemical abundances for 14 elements (C, O, Na, Mg, Al, Si, K, Ca, Ti, V, Cr, Mn, Fe, and Ni) are derived for a sample of M dwarfs using high-resolution, near-infrared *H*-band spectra from the Sloan Digital Sky Survey-IV/Apache Point Observatory Galactic Evolution Experiment (APOGEE) survey. The quantitative analysis included synthetic spectra computed with 1D LTE plane-parallel MARCS models using the APOGEE Data Release 17 line list to determine chemical abundances. The sample consists of 11 M dwarfs in binary systems with warmer FGK dwarf primaries and 10 measured interferometric angular diameters. To minimize atomic diffusion effects, [X/Fe] ratios are used to compare M dwarfs in binary systems and literature results for their warmer primary stars, indicating good agreement (<0.08 dex) for all studied elements. The mean abundance difference in primaries minus this work's M dwarfs is -0.05 ± 0.03 dex. It indicates that M dwarfs in binary systems are a reliable way to calibrate empirical relationships. A comparison with abundance, effective temperature, and surface gravity results from the APOGEE Stellar Parameter and Chemical Abundances Pipeline (ASPCAP) Data Release 16 finds a systematic offset of [M/H], $T_{\rm eff}$, log $g = +0.21$ dex, -50 K, and 0.30 dex, respectively, although ASPCAP [X/Fe] ratios are generally consistent with this study. The metallicities of the M dwarfs cover the range of [Fe/H] $= -0.9$ to $+0.4$ and are used to investigate Galactic chemical evolution via trends of [X/Fe] as a function of [Fe/H]. The behavior of the various elemental abundances [X/Fe] versus [Fe/H] agrees well with the corresponding trends derived from warmer FGK dwarfs, demonstrating that the APOGEE spectra can be used to examine Galactic chemical evolution using large samples of selected M dwarfs.

Unified Astronomy Thesaurus concepts: Near infrared astronomy (1093); M dwarf stars (982); Stellar abundances (1577); Wide binary stars (1801); Exoplanets (498)

1. Introduction

M dwarfs are low-mass stars (the lowest mass M dwarfs falling just above the hydrogen-burning limit), with small radii, and comprise roughly 70% of Galactic stellar populations (Miller & Scalo 1979; Henry et al. 2018). Because of their relatively small masses and sizes, M dwarfs are intrinsically faint stars that are challenging to study at large distances using currently available telescopes; nonetheless, due to their large numbers, a great many M dwarfs in the solar neighborhood have been studied in the optical and near-infrared (NIR) at both low and high spectral resolutions.

The optical spectra of M dwarfs contain several strong molecular absorption features (e.g., TiO or VO; Allard et al. 2000) which limit the use of "well-known" spectral analysis techniques that are used typically in high-resolution abundance studies of the warmer FKG main-sequence stars. Despite this difficulty, a number of works using optical lines that are likely free of molecular blends (e.g., Woolf & Wallerstein 2005;

Bean et al. 2006; Woolf & Wallerstein 2020) have shown that it is possible to derive individual abundances of Fe, Ca, and Ti via spectrum-synthesis analyses of high-resolution optical M-dwarf spectra. Also using high-resolution optical spectra, Chavez & Lambert (2009) derived $^{46}Ti/^{50}Ti$ isotopic ratios in 11 M dwarfs in the Galactic halo and disk (thin and thick), as well as analyzing TiO lines to confirm their metallicity scale. Veyette et al. (2017) used equivalent widths of Fe I and Ti I lines from *Y*-band spectra to produce a calibration for $T_{\rm eff}$, [Fe/H], and [Ti/Fe], achieving an internal precision of 60 K, 0.10, and 0.05 dex, respectively, in their results, which are typical of those obtained for the warmer F, G, and K stars.

Studying M dwarfs in the NIR brings two main advantages to the analysis: they are much brighter in the NIR than in the optical, and, in general, the NIR spectra of M dwarfs have fewer strong molecular blends than in their optical spectra. Although molecular lines of CO, H_2O, and FeH are present in the NIR, their absorption is not as dense and deep; note, however, that millions of water lines in the Apache Point Observatory Galactic Evolution Experiment (APOGEE; Majewski et al. 2017) *H* band become dominant for M dwarfs with low effective temperatures ($T_{\rm eff} \leqslant 3500$ K). In the previous works of Tsuji & Nakajima (2014), Tsuji et al. (2015), and Tsuji & Nakajima (2016), C and O abundances were determined via spectral syntheses in the *K* band using the molecular lines of CO and H_2O. Also using the *K* band, Rojas-Ayala et al. (2012) developed a spectroscopic calibration based on equivalent widths of Na I and Ca I lines to determine M-dwarf metallicities (see also Covey et al. 2010; Rojas-Ayala et al. 2010; Mann et al. 2013b; Newton et al. 2014; Terrien et al. 2015).

From high-resolution *J*-band spectra, Lindgren et al. (2016) and Lindgren & Heiter (2017) demonstrated that FeH and Fe I lines can be used to determine precise exoplanet-hosting M-dwarf metallicities via spectrum synthesis. The Calar Alto high-Resolution search for M dwarfs with Exo-earths with Near-infrared and optical Echelle Spectrographs (CARMENES) and Habitable-Zone Planet Finder surveys (Mahadevan et al. 2012; Quirrenbach et al. 2014) obtain high-resolution spectra covering both NIR and optical spectral regions: this spectral combination constitutes one of the most powerful tools to characterize M-dwarf spectra (Passegger et al. 2018; Reiners et al. 2018). From an analysis of CARMENES spectra in the region between roughy λ9000–13,000 Å, Ishikawa et al. (2020) determined abundances of eight elements for a sample of five M dwarfs in binary systems. Ishikawa et al. (2022) used Subaru/IRD high-resolution spectra to determine detailed chemical abundances for 13 M dwarfs.

The high-resolution spectroscopic APOGEE survey has also opened a new window into the chemical analysis and stellar characterization of significant numbers of M dwarfs in the Milky Way. Using different approaches, Rajpurohit et al. (2018), Birky et al. (2020), Souto et al. (2020), and Sarmento et al. (2021) determined the atmospheric parameters and metallicities of APOGEE M dwarfs, while previous work by Souto et al. (2017, 2018) demonstrated proof-of-concept analysis techniques that yielded individual abundances for more than 10 chemical elements from the *H*-band APOGEE spectra.

In this work we present a detailed chemical abundance study for a sample of 21 M dwarf stars. We determined the chemical abundances of 14 elements covering different nucleosynthetic origins: C (produced primarily in low- to intermediate-mass stars); the α-elements O, Mg, Si, and Ca; the odd-*Z* elements Na, Al, and K; and the iron-peak elements Cr, Mn, Fe, and Ni: all derived using the APOGEE spectra and an updated APOGEE line list (Smith et al. 2021). The targets were taken from our previous studies (Souto et al. (2020, 2021)), as they could serve as benchmark stars for metallicity and effective temperature calibrations and validations. Here, with the addition of detailed chemistry for these targets, which are for the most part solar neighborhood M-dwarf members of binary systems, or benchmarks with measured angular diameters, we can begin to compare chemical abundances for M dwarfs with other populations in the Milky Way and investigate their behavior in the canonical [X/Fe] versus [Fe/H] plane. The M-dwarf abundances can also be used to calibrate results in Data Release 16 (DR16), which were derived automatically using the APOGEE Stellar Parameter and Chemical Abundances Pipeline (ASPCAP; Jönsson et al. 2020). Section 2 of this paper presents the studied sample, Section 3 the abundance analysis and the determination of the stellar parameters. In Section 4, we discuss the results, and summarize them in Section 5.

2. The Data and the Sample

The M dwarfs analyzed here were taken from Souto et al. (2020) and Souto et al. (2021). This sample contains 11 M dwarf stars in wide binary systems with warmer primaries selected from Mann et al. (2013a) and Montes et al. (2018), along with 10 field M dwarfs with interferometric radii measured by Boyajian et al. (2012).

The targets were observed as part of the APOGEE-1/Sloan Digital Sky Survey-IV (SDSS-IV; Blanton et al. 2017) from observations using the APOGEE-N spectrograph, a multifiber (300) high-resolution ($R = \lambda/\Delta\lambda \sim 22{,}500$; Gunn et al. 2006; Wilson et al. 2019) cryogenic spectrograph operating in the NIR *H* band (λ1.51–1.69 μm) and located at the Apache Point Observatory (New Mexico, USA). Here, we use updated reduced spectra for the sample (Nidever et al. 2015) from the publicly available 16th SDSS data release (DR16; Ahumada et al. 2020; Jönsson et al. 2020).

3. Stellar Parameters and Abundance Analysis

The effective temperatures ($T_{\rm eff}$), surface gravities (log *g*), metallicities ([Fe/H]), along with carbon (A(C)) and oxygen (A(O)) abundances for the studied stars were determined using solutions to $T_{\rm eff}$–A(O) pairs and log *g*–A(O) pairs; the method consists in deriving oxygen abundances from different abundance indicators (OH and H_2O lines) as functions of $T_{\rm eff}$ and log *g*. This procedure leads to a unique value of $T_{\rm eff}$ and log *g* yielding the same oxygen abundance derived from the different oxygen abundance indicators. We refer the reader to Souto et al. (2020) for more details on the methodology.

The abundance calculations are based on the 1D plane-parallel LTE MARCS model atmospheres (Gustafsson et al. 2008), the turbospectrum code (Alvarez & Plez 1998 and Plez 2012) and the BACCHUS wrapper (Masseron et al. 2016) in the manual mode. Synthetic spectra were generated using the most recent version of the APOGEE line list (Smith et al. 2021), which was also used in Data Release 17. We determined chemical abundances via comparisons of synthetic and observed spectra.

Table 1
Stellar Parameters

2Mass ID	ID	*J*	*H*	*Ks*	d (pc)	$T_{\rm eff}$	log *g*	[Fe/H]
Binaries								
2M03044335+6144097	GJ 3195	8.877	8.328	8.103	23.5	3541	4.72	−0.33
2M03150093+0103083	NLTT 10349	11.622	11.043	10.855	77.5	3672	4.69	−0.92
2M03553688+5214291	LSPM J0355+5214	10.885	10.325	10.127	39.6	3455	4.89	−0.34
2M06312373+0036445	NLTT 16628	11.077	10.465	10.252	72.1	3752	4.70	−0.39
2M08103429-1348514	GJ 9255 B	8.276	7.672	7.418	20.9	3566	4.76	0.01
2M12045611+1728119	LSPM J1204+1728S	9.793	9.183	8.967	37.6	3369	4.82	−0.45
2M14045583+0157230	NLTT 36190	10.129	9.483	9.269	51.8	3630	4.65	0.05
2M18244689-0620311	PM J18247-0620	9.659	9.052	8.795	39.6	3425	4.77	0.05
2M20032651+2952000	GJ 777 B	9.554	9.026	8.712	16.0	3295	5.05	0.21
2M02361535+0652191	GJ 105 B	7.333	6.793	6.574	7.2	3335	4.95	−0.20
2M05413073+5329239	GJ 212	6.586	5.963	5.759	12.3	3783	4.74	0.21
Interferometric radii								
2M11032023+3558117	GJ 411	4.203	3.640	3.254	2.6	3579	4.81	−0.44
2M11052903+4331357	GJ 412 A	5.538	5.002	4.769	4.8	3567	4.84	−0.49
2M00182256+4401222	GJ 15 A	5.252	4.476	4.018	3.6	3585	4.85	−0.39
2M05312734-0340356	GJ 205	4.999	4.149	4.039	5.7	3820	4.67	0.29
2M09142298+5241125	GJ 338 A	4.889	3.987	3.988	6.3	3931	4.66	0.02
2M09142485+5241118	GJ 338 B	4.779	4.043	4.136	6.3	3870	4.70	0.11
2M13454354+1453317	GJ 526	5.181	4.775	4.415	5.4	3714	4.71	−0.36
2M18424666+5937499	GJ 725 A	5.189	4.741	4.432	3.5	3505	4.84	−0.34
2M18424688+5937374	GJ 725 B	5.721	5.197	5.000	3.5	3400	4.90	−0.36
2M22563497+1633130	GJ 880	5.36	4.800	4.253	6.9	3643	4.78	0.26

Note. The estimated uncertainties in $T_{\rm eff}$, log *g*, and [Fe/H] are about 100K, 0.20 dex, and 0.10 dex, respectively.

Individual abundances were measured, whenever possible, for a total 113 spectral lines: 15 lines of Fe I, 25 of FeH, 2 of CO, 4 of H_2O, 32 of OH, 2 of Na I, 3 of Mg I, 3 of Al I, 4 of Si I, 2 of K I, 3 of Ca I, 6 of Ti I, 1 of V I, 1 of Cr I, and 3 of Mn I, based on Souto et al. (2018; stars with $T_{\rm eff} < 3500$ K) and Souto et al. (2017; stars with $T_{\rm eff} > 3500$ K). In this work, we add seven Ni I lines at air wavelengths of λ15605.7 Å, λ15632.7 Å, λ16584.4 Å, λ16589.3 Å, λ16673.7 Å, λ16815.5 Å, and λ16818.8 Å, which are measurable in the APOGEE spectra of metal-rich M dwarfs but were not previously studied in Souto et al. (2017) and Souto et al. (2018), as these lines are very weak for solar and subsolar metallicities. The Ti and V abundances derived here displayed an unexpected trend as a function of metallicity. Therefore, we remove these species from the Discussion section as work needs to be done to determine what is driving this offset. The adopted atmospheric parameters and the derived individual abundances are presented in Tables 1 and 2, respectively.

Figure 1 shows the APOGEE spectra (from $\sim \lambda$1.5 to 1.7 μm) for two M dwarfs in our sample. The two selected stars have similar stellar parameters ($T_{\rm eff}$ and log *g*) but different metallicities; while 2M14045583+0157230 has a solar metallicity (red line), 2M03150093+0103083 is metal-poor ([Fe/H] ~ -1.0; blue line). It is apparent from a comparison of their spectra that the overall shape of both spectra is similar, which is driven by the similarity of their $T_{\rm eff}$ and log *g* values. However, the strengths of the absorption lines are shallower/weaker for several species in the metal-poor star. This behavior is more prominent for the neutral atomic lines.

Figure 2 presents an expansion of the region in Figure 1 containing four lines: from left to right, λ15294.4 Å Fe I, the λ15334.8 Å Ti I, the λ15632.0 Å Ni I, and λ15258.1 Å H_2O. In the metal-poor M dwarf, the neutral lines have absorption depths with roughly 10%–15% lower values when compared to the solar-metallicity M dwarf, while the OH lines display roughly the same depths for both stars, and the H_2O lines in the metal-poor star are stronger than those in the solar-metallicity one, which is expected if the metal-poor star has an enhanced value of [O/Fe].

3.1. Abundance Uncertainties

The uncertainties in the derived abundances in this work are estimated to be the same as in our previous investigations, given the similarities in the adopted analysis methodologies. For the early M dwarfs ($T_{\rm eff} > 3500$ K) we refer to the uncertainties presented in Souto et al. (2017), and for the mid-type M dwarfs ($T_{\rm eff} < 3500$ K), see Souto et al. (2018). The uncertainties in the derived atmospheric parameters are the same as the ones presented in Souto et al. (2020): $\pm$100 K and $\pm$0.16 dex for $T_{\rm eff}$ and log *g*, respectively.

4. Results and Discussion

Stellar parameters and iron abundances for the stars in this study were previously derived in Souto et al. (2020). However, this previous study used spectra from a previous version of the APOGEE data reduction pipeline (Jönsson et al. 2020), along with a previous version of the line list (Shetrone et al. 2015), while here we adopt the most recent APOGEE line list that has several updates (Smith et al. 2021). A comparison of the stellar parameters and metallicities obtained with those derived previously from the same APOGEE spectra finds good agreement: delta $T_{\rm eff} = 16 \pm 56$ K; delta log $g = 0.00 \pm 0.10$ dex, and delta [Fe/H] $= 0.10 \pm 0.04$ dex. Assuming only the interferometric stars, we obtain delta $T_{\rm eff} = 8 \pm 79$ K and delta log $g = 0.03 \pm 0.10$ dex. In this study the derived metallicities are the mean of the iron abundances from the Fe I and FeH lines, while Souto et al. (2020) used only Fe I lines as their metallicity indicator (see discussion in Souto et al. 2021).

Table 2
Stellar Abundances

Element	4097	3083	4291	6445	8514	8119	7230	0311	2000	2191	9239	8117	1357	1222	0356	1125	1118	3317	7499	7374	3130
⟨A(Fe[Fe i])⟩	7.20	6.55	7.16	7.09	7.50	7.05	7.54	7.50	7.70	7.32	7.69	7.05	7.05	7.10	7.81	7.52	7.59	7.14	7.10	7.13	7.81
⟨A(Fe[FeH])⟩	7.04	6.51	7.06	7.04	7.43	6.95	7.47	7.50	7.62	7.18	7.63	6.97	6.87	7.03	7.67	7.42	7.52	7.04	7.12	7.05	7.61
⟨A(C)⟩	8.20	7.62	8.03	8.10	8.34	8.01	8.40	8.36	8.62	8.29	8.55	8.04	7.92	7.96	8.65	8.26	8.32	8.24	8.18	8.19	8.58
⟨A(O[H2O])⟩	8.58	8.21	8.39	8.47	8.62	8.31	8.65	8.66	8.86	8.61	8.80	8.44	8.30	8.33	8.89	8.52	8.60	8.59	8.54	8.52	8.80
⟨A(O[OH])⟩	8.60	8.20	8.40	8.48	8.62	8.30	8.65	8.68	8.86	8.63	8.76	8.44	8.32	8.34	8.85	8.56	8.58	8.57	8.53	8.55	8.80
⟨A(Na)⟩	5.95	⋯		5.80	6.17	⋯	6.25	6.19	⋯		6.27	⋯		⋯	6.71	6.14	⋯		⋯		6.55
⟨A(Mg)⟩	7.62	7.11	7.33	7.29	7.62	7.27	7.58	7.72	7.55	7.56	7.60	7.37	7.35	7.38	7.74	7.41	7.56	7.39	7.29	7.51	7.95
⟨A(Al)⟩	6.22	5.62	5.95	5.95	6.24	5.84	6.32	6.39	6.50	6.19	6.37	6.01	5.96	6.02	6.60	6.17	6.30	6.11	6.07	6.24	6.77
⟨A(Si)⟩	7.37	6.83	7.24	7.25	7.47	⋯	7.52	⋯		⋯	7.61	7.22	7.17	7.35	7.75	7.45	7.58	7.28	7.16	⋯	7.89
⟨A(K)⟩	4.97	4.42	4.82	4.80	4.99	4.64	5.04	5.04	5.22	4.93	5.07	4.68	4.67	4.71	5.31	4.93	4.95	4.88	4.85	4.77	5.25
⟨A(Ca)⟩	6.29	5.76	6.06	6.14	6.39	6.02	6.33	6.40	6.39	6.32	6.45	6.08	6.07	6.16	6.59	6.27	6.28	6.13	6.10	6.15	6.60
⟨A(Cr)⟩	⋯		⋯	5.33	5.65	⋯	5.70	⋯		⋯	5.87	⋯		⋯	6.08	5.66	5.72	⋯		⋯	6.04
⟨A(Mn)⟩	5.09	⋯		4.83	5.40	⋯	5.36	⋯		⋯	5.49	4.78	4.85	4.90	5.70	5.25	5.33	4.98	⋯		5.68
⟨A(Ni)⟩	⋯		⋯		⋯		⋯		⋯		6.42	⋯		⋯	6.68	6.28	6.39	⋯		⋯	⋯

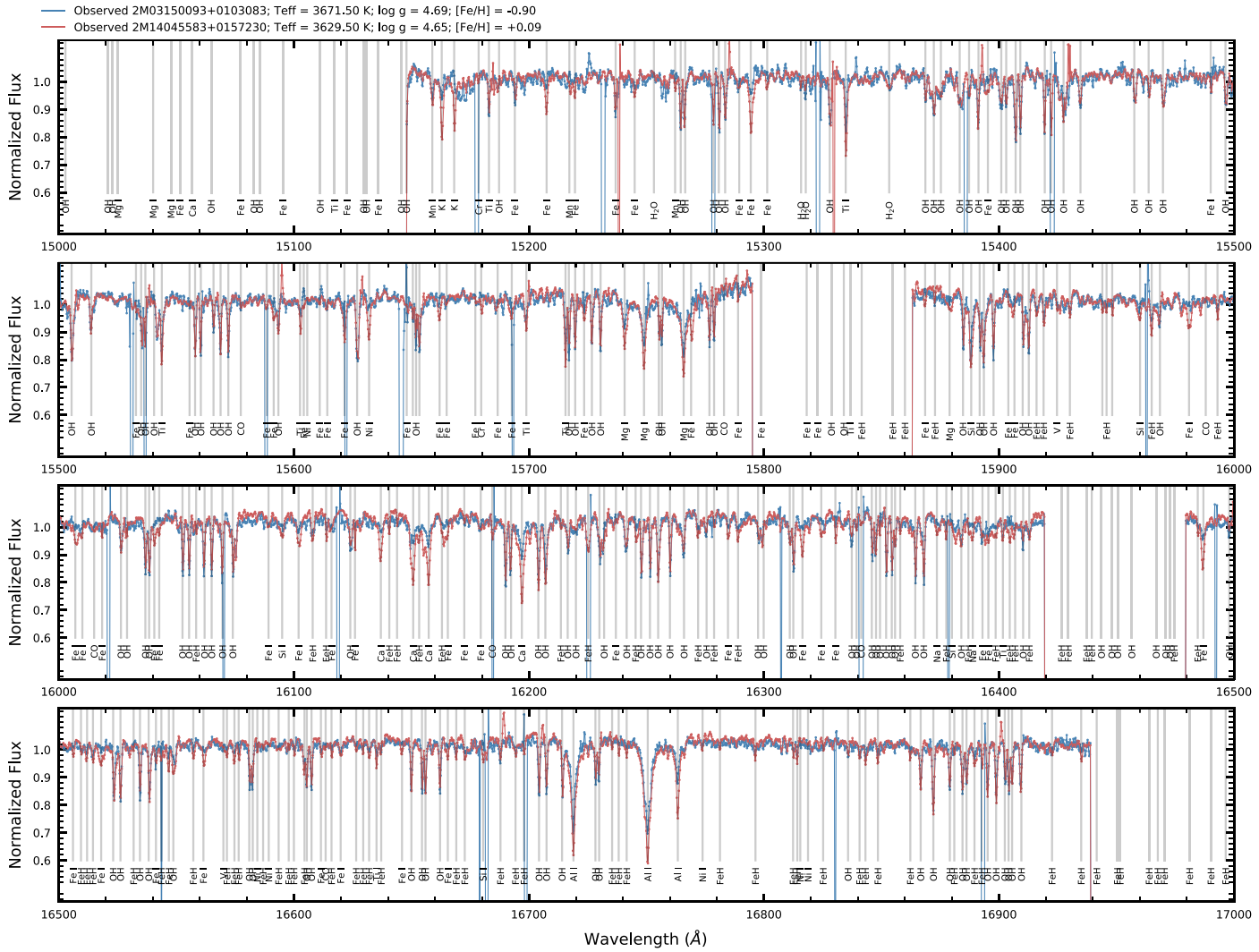

Figure 1. Line identification in the normalized APOGEE spectra of a solar metallicity (2M14045583+0157230) and a metal-poor (2M03150093+0103083) M dwarf, represented as red and blue lines, respectively. All spectral lines available in the M-dwarf APOGEE spectra are shown as gray lines.

Three stars of this work have detected exoplanets: GJ 411, GJ 15 A, and GJ 338 B. GJ 411 hosts a "mass-like" Earth with $M_{\oplus}{}^{*}\sin(i) = 2.69$, equilibrium temperature ($T_{\rm eq}$) and insolation flux ($S_{\oplus}$) of 370 K and 3.13, respectively (Stock et al. 2020). GJ 15 A has two exoplanets detected to date (Pinamonti et al. 2018), where GJ 15 A b is considerably less massive than GJ 15 A c, $M_{\oplus}{}^{*}\sin(i) = 3.03$ and 36. GJ 338 B likely hosts a super-Earth, where GJ 338 B b has $M_{\oplus}{}^{*}\sin(i) = 10.27$ and $T_{\rm eq} = 391$ K (González-Álvarez et al. 2020). These four exoplanets were detected by radial velocity, and no transit observations are available to date. This work's abundance results can be used to study the star–planet connection and geophysical properties of these likely rocky exoplanets in future works.

4.1. Verifying the Abundance Scale Using M Dwarfs in Binary Systems

As discussed previously, M dwarfs that are members of wide binary systems provide an opportunity to compare their abundances with those for the warmer primaries, which can be obtained from a number of studies in the literature (Bonfils et al. 2005; Mann et al. 2013a; Montes et al. 2018; Ishikawa et al. 2020). There remains one caveat in the use of binary systems as abundance tests for M dwarfs: the assumption that the chemical compositions of the M dwarf and its primary are identical. The process of atomic diffusion will alter the surface abundances, to varying degrees, of main-sequence stars over time (Michaud et al. 2015), with heavy elements diffusing downward, out of the outer convective envelope, relative to H, thus lowering values of [X/H] in the photosphere relative to their initial values on the zero age main sequence. The magnitude of the abundance changes wrought by diffusion are strong functions of stellar mass and age, with changes being of the order of 0.01 to ∼0.1 dex. Atomic diffusion has been observed in the abundance distributions in the open clusters M67 (Bertelli Motta et al. 2018; Gao et al. 2018; Souto et al. 2018, 2019), NGC 2420 (Semenova et al. 2020), and Coma Berenices (Souto et al. 2021). As M dwarfs have relatively massive and deep convective envelopes, when compared to hotter (and more massive) main-sequence stars, diffusion effects are much reduced. In a binary system consisting of an M dwarf and a hotter and more massive FGK primary, diffusion will act preferentially over time to reduce the heavy-element abundances in the primary relative to the M-dwarf companion.

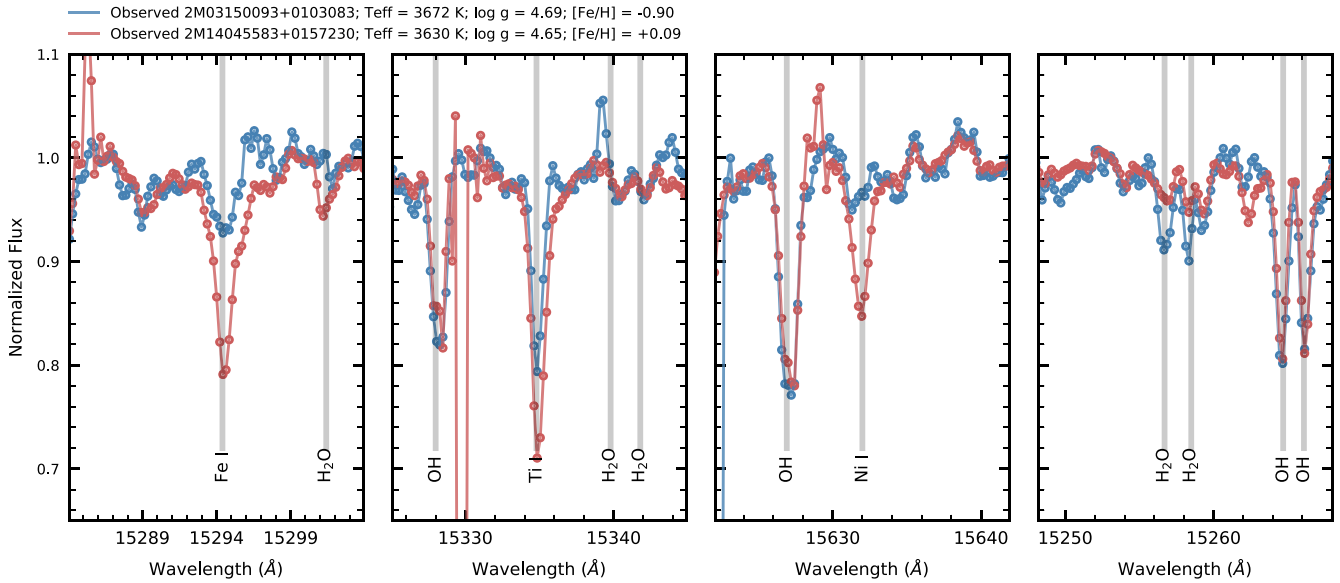

Figure 2. Expanded views of four lines in Figure 1. The panels display the λ15294.4 Å Fe I, λ15334.8 Å Ti I, λ15632.0 Å Ni I, and λ15258.1 Å H_2O, from left to right, respectively.

The warm primaries in this study cover a range in effective temperature from roughly 4600–6300 K and, in principle, they would experience varying levels of diffusion (0.01 to 0.12 dex assuming solar age; Choi et al. 2016). However, even if the amount of diffusion that the primaries suffer is unknown, diffusion effects are roughly similar for the different elements studied (Pinsonneault et al. 1989; Choi et al. 2016; Dotter et al. 2017), and this similar behavior can be used in the form of [X/Fe] ratios, which, to a degree, removes and minimizes diffusion effects. We emphasize, however, that we do not aim to measure diffusion effects in binary systems. We are simply analyzing the El/Fe ratio, which would tend to erase diffusion signatures (if they exist), as all elements are affected by roughly the same level of photospheric abundance depletion (Choi et al. 2016).

Comparisons of our M-dwarf [X/Fe] results with literature values of [X/Fe] for the primaries for 10 elements are shown in the top panels of Figure 3, and the offsets are summarized in Table 3. The mean differences between the elemental abundances-relative-to-iron of the primary stars minus M dwarfs in this work (along with standard deviations) are labeled in the top left of each panel (see Table 3). The bottom panels of the figure display the corresponding residual diagram ([X/Fe] (warm primaries) − [X/Fe] (M dwarfs)) plotted as a function of our derived effective temperature. Overall, these abundances for the M dwarfs are in good/reasonable agreement with the comparison values from the literature (see Table 3). The comparison of individual elemental abundances between the M dwarfs and their companion primary stars is limited for many of the elements by published elemental abundances for the primaries. The elements K and Cr, for example, do not have literature results for the primary stars.

The iron abundances are presented relative to H (top-left panel of Figure 3), and therefore could be affected to some level by diffusion (see Dotter et al. 2017). Possible effects of diffusion aside, there is almost no offset between the mean abundances: $\langle$[Fe/H] (this work) − [Fe/H] (warm primaries)$\rangle = +0.02 \pm 0.13$ dex. (Souto et al. 2020 used an older APOGEE line list and found a slightly different mean metallicity difference by 0.02 dex.) Iron is the best-represented abundance in the comparisons, as all 11 binary systems have published values of [Fe/H]. The standard deviation of the mean for [Fe/H] of $\pm$0.13 dex is a typical level of dispersion found in abundance analyses, given that all abundances carry some level of systematic uncertainties and internal errors, and because they come from different methodologies and literature sources (see Hinkel et al. 2014).

The elements O, Mg, Si, and Ca are also represented by more than just a few comparison binary systems ($N \geqslant 4$). Using values of [X/Fe] as references for the abundance comparisons, the differences are quite small and the standard deviations are 0.14 dex and below, as can be seen in Figure 3. The mean abundance differences in "Primaries − M dwarfs" is -0.05 ± 0.03 dex. Taken together, the results for the O, Mg, Si, and Ca indicate that there are no significant trends between the M-dwarf abundance scale and the warmer FGK companion stars.

The remaining elements are represented in the binary sample by only small numbers of comparisons, so any underlying trends in the M-dwarf abundances would be difficult to discern, unless they are systematic and large. For example, only two sample stars had carbon abundance results in the literature for their primaries. The mean abundance difference (M dwarf − Primary) is $\delta = 0.01 \pm 0.01$ dex. Aluminum and sodium also had only two or three comparison systems each, with no striking conclusions to be drawn, other than that there are no large differences found.

The final two elements to be discussed are Mn and Ni, where only one literature result for the primary stars is found to compare with the M-dwarf abundance. These elements are included largely for completeness: the differences for these single comparisons of δ [Mn/Fe] = 0.05, and δ [Ni/Fe] = −0.04 dex.

4.2. Comparison With DR16 ASPCAP Results

The main goal of the APOGEE survey is the determination of chemical abundances in Galactic red-giant stars; this task relies on the APOGEE ASPCAP pipeline (García Pérez et al. 2016), which automatically derives stellar parameters and chemical abundances for more than 25 species. In this context, the ASPCAP pipeline has been optimized to analyze red giants

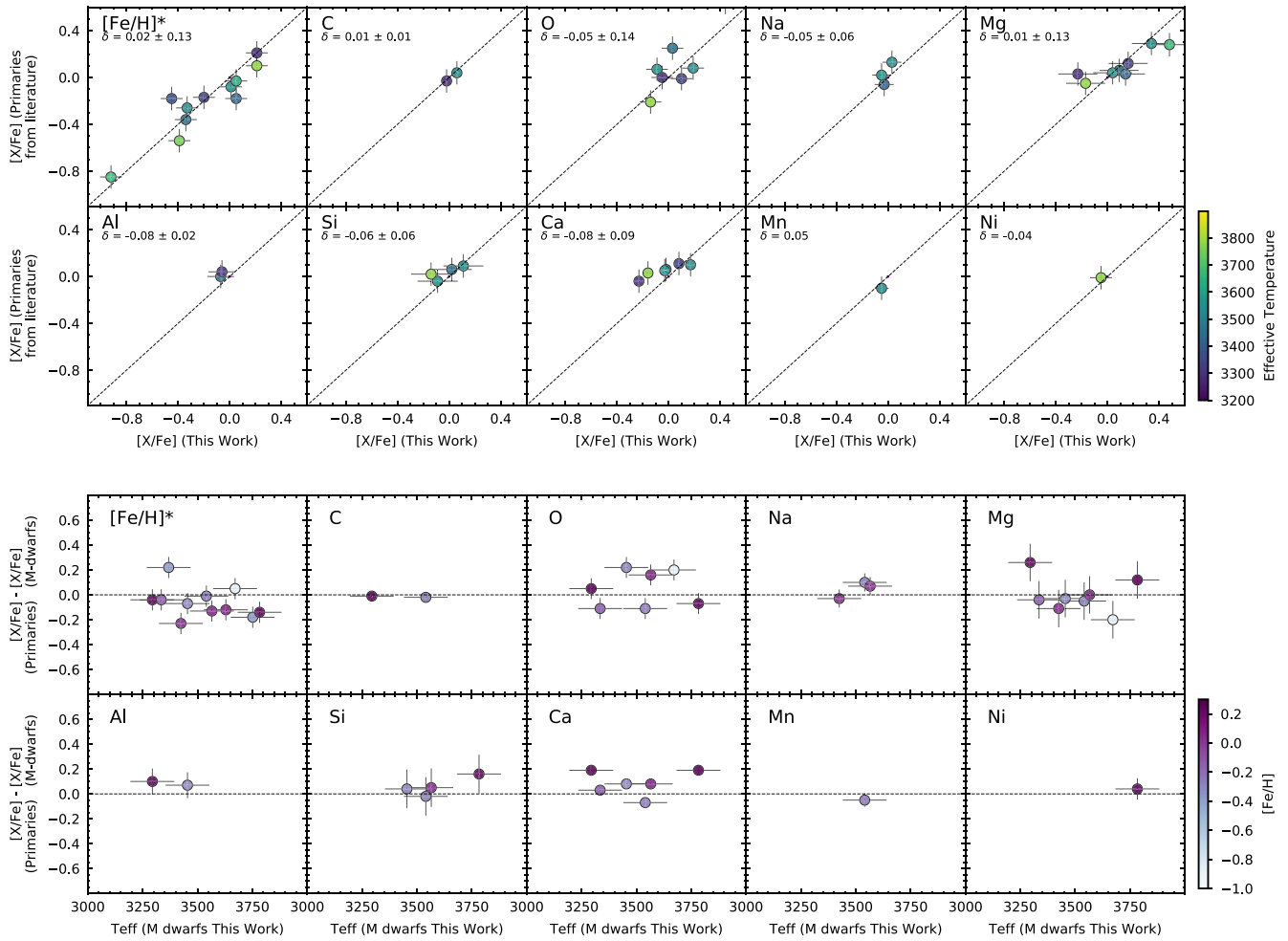

Figure 3. Top panels: comparison of the [X/Fe] abundances in binary systems containing an M dwarf and a warmer primary of type FGK. Bottom panels: the residual [X/Fe] (primaries) − [X/Fe] (M dwarfs) vs. the M-dwarf effective temperatures. For iron we adopt [Fe/H] instead of [X/Fe].

and not M dwarfs. ASPCAP determines stellar parameters and chemical abundances in two distinct phases. First, seven parameters ($T_{\rm eff}$, log g, [M/H], [C/Fe], [N/Fe], [α/Fe], and the microturbulent velocity) are derived via a 7D chi-squared minimization over the entire wavelength range of the APOGEE spectra. In a second step, ASPCAP uses the atmospheric parameters from step one and derives the individual abundances by minimizing differences in selected spectral windows (or pixels) that are sensitive to the respective elemental abundances.

In the earlier APOGEE data releases (DR10, Ahn et al. 2014; DR12, Alam et al. 2015), the atmospheric parameters and chemical abundances of the relatively small number of M dwarfs observed by APOGEE were not reliable due to the lack of model atmospheres and synthetic models for M dwarfs in the ASPCAP libraries (Zamora et al. 2015). In addition, the line lists for H_2O (Barber et al. 2006) and FeH (Hargreaves et al. 2010), which are crucial for modeling M dwarfs, were only introduced in DR14 (Abolfathi et al. 2018) and DR16, respectively. DR16 had adequate line lists and model atmospheres grids, with $T_{\rm eff}$ ranging from 3000–4000K, log g from +2.5–+5.5 dex, and [Fe/H] from −2.5–+1.00 dex, as presented by Jönsson et al. (2020) However, the abundance windows in ASPCAP remained optimized for red giants, and this most recent data release still lacks abundance windows dedicated to M dwarf stars.

A comparison between the values of $T_{\rm eff}$ and log g derived here for the M dwarfs with those from APOGEE DR16 are presented in the top and bottom panels of Figure 4, respectively. This comparison includes both the ASPCAP raw results (left panels) and calibrated ones (right panels; see Jönsson et al. 2020); at the bottom of each panel, residual diagrams as functions of $T_{\rm eff}$ and log g are displayed. There is good agreement between our $T_{\rm eff}$ scale and that of the DR16 ASPCAP raw, where $\langle T_{\rm eff,\ this\ work} - T_{\rm eff,\ DR16}\rangle = -50 \pm 67$ K. This offset is smaller than the nominal uncertainties in $T_{\rm eff}$, indicating that it is probably not statistically significant. The calibrated $T_{\rm eff}$ from the DR16, conversely, show a more significant systematic offset when compared to our results: $\langle T_{\rm eff,\ this\ work} - T_{\rm eff,\ DR16}\rangle = -156 \pm 62$ K.

Concerning the surface gravity comparison, we can see from Figure 4 (bottom-left panel) that many of the raw ASPCAP log g values spread around log $g \sim 4.8$, with some of the values being significantly lower (∼4.4–4.1). If we simply compare the mean of the difference we obtain a significant offset and scatter: $\langle \log g_{\rm this\ work} - \log g_{\rm DR16}\rangle = -0.30 \pm 0.29$ dex. However, this difference is quite log g dependent, as shown by the residual diagram in the bottom-left panel of Figure 4; for the coolest M dwarf stars in the sample ($T_{\rm eff} < 3400$K), the difference $\langle \log g_{\rm this\ work} - \log g_{\rm DR16}\rangle$ can reach up to ∼+0.9 dex. One star that deviates from this systematic trend is 2M12045611+1728119, for which the surface gravity value

Table 3
Abundance Ratios

M Dwarfs Secondary Warmer Primaries	4097 HIP 14286	3083 HIP 15126	4291 HIP 18366	6445 HIP 31127	8514 HIP 40035	8119 HIP 58919	7230 HIP 68799	0311 HIP 90246	2000 HIP 98767	2191 HIP 12114	9239 HIP 26779
⟨[Fe/H]⟩ (M dwarfs)	−0.33	−0.92	−0.34	−0.39	0.01	−0.45	0.05	0.05	0.21	−0.20	0.21
⟨[Fe/H]⟩ (Warmer primaries)	−0.26	−0.85	−0.36	−0.54	−0.08	−0.18	−0.03	−0.18	0.21	−0.17	0.10
δ (M dwarfs − warmer primaries)	−0.07	−0.07	0.02	0.15	0.09	−0.27	0.08	0.23	0.00	−0.03	0.11
⟨[C/Fe]⟩ (M dwarfs)	0.14	0.15	−0.02	0.09	−0.07	0.07	−0.04	−0.08	0.02	0.10	−0.05
⟨[C/Fe]⟩ (Warmer primaries)	0.04	⋯	⋯	⋯	⋯	⋯	⋯	⋯	−0.03	⋯	
δ (M dwarfs − warmer primaries)	0.10	⋯	⋯	⋯	⋯	⋯	⋯	⋯	0.05	⋯	
⟨[O/Fe]⟩ (M dwarfs)	0.27	0.46	0.08	0.21	−0.06	0.09	−0.06	−0.03	−0.01	0.17	−0.11
⟨[O/Fe]⟩ (Warmer primaries)	0.08	0.64	0.25	⋯	0.07	⋯	⋯	⋯	0.00	−0.01	−0.21
δ (M dwarfs − warmer primaries)	0.19	−0.18	−0.17	⋯	−0.13	⋯	⋯	⋯	−0.01	0.18	0.10
⟨[Na/Fe]⟩ (M dwarfs)	0.11	⋯	⋯	0.02	−0.01	⋯	0.03	−0.03	⋯	⋯	−0.11
⟨[Na/Fe]⟩ (Warmer primaries)	0.13	0.02	−0.04	⋯	0.02	⋯	⋯	−0.06	0.03	⋯	
δ (M dwarfs − warmer primaries)	−0.02	⋯	⋯	⋯	−0.03	⋯	⋯	0.03	⋯	⋯	
⟨[Mg/Fe]⟩ (M dwarfs)	0.42	0.50	0.14	0.15	0.08	0.19	0.00	0.14	−0.19	0.23	−0.14
⟨[Mg/Fe]⟩ (Warmer primaries)	0.29	0.28	0.06	⋯	0.04	⋯	⋯	0.03	0.03	0.12	−0.05
δ (M dwarfs − warmer primaries)	0.13	0.22	0.08	⋯	0.04	⋯	⋯	0.11	−0.22	0.11	−0.09
⟨[Al/Fe]⟩ (M dwarfs)	0.18	0.17	−0.08	−0.03	−0.15	−0.08	−0.11	−0.03	−0.08	0.02	−0.21
⟨[Al/Fe]⟩ (Warmer primaries)	⋯	⋯	0.00	⋯	⋯	⋯	⋯	⋯	0.04	⋯	
δ (M dwarfs − warmer primaries)	⋯	⋯	−0.08	⋯	⋯	⋯	⋯	⋯	−0.12	⋯	
⟨[Si/Fe]⟩ (M dwarfs)	0.19	0.24	0.07	0.13	−0.05	⋯	−0.04	⋯	⋯	⋯	−0.11
⟨[Si/Fe]⟩ (Warmer primaries)	0.09	⋯	0.06	⋯	−0.04	⋯	⋯	0.07	0.09	⋯	0.02
δ (M dwarfs − warmer primaries)	0.10	⋯	0.01	⋯	−0.01	⋯	⋯	⋯	⋯	⋯	−0.13
⟨[Ca/Fe]⟩ (M dwarfs)	0.31	0.37	0.09	0.22	0.07	0.16	−0.03	0.04	−0.13	0.21	−0.07
⟨[Ca/Fe]⟩ (Warmer primaries)	0.10	⋯	0.06	⋯	0.05	⋯	⋯	⋯	−0.04	0.11	0.03
δ (M dwarfs − warmer primaries)	0.21	⋯	0.03	⋯	0.02	⋯	⋯	⋯	−0.09	0.10	−0.10
⟨[Mn/Fe]⟩ (M dwarfs)	0.03	⋯	⋯	−0.17	0.00	⋯	−0.08	⋯	⋯	⋯	−0.11
⟨[Mn/Fe]⟩ (Warmer primaries)	−0.10	⋯	⋯	⋯	⋯	⋯	⋯	⋯	⋯	⋯	
δ (M dwarfs − warmer primaries)	0.13	⋯	⋯	⋯	⋯	⋯	⋯	⋯	⋯	⋯	
⟨[Ni/Fe]⟩ (M dwarfs)	⋯	⋯	⋯	⋯	⋯	⋯	⋯	⋯	⋯	⋯	−0.02
⟨[Ni/Fe]⟩ (Warmer primaries)	0.03	⋯	0.00	⋯	0.01	⋯	⋯	−0.10	0.05	⋯	−0.01
δ (M dwarfs − warmer primaries)	⋯	⋯	⋯	⋯	⋯	⋯	⋯	⋯	⋯	⋯	−0.01

Note. Adopted abundances from the literature are from Shi et al. (2004), Soubiran & Girard (2005), Reddy et al. (2006), Mishenina et al. (2008, 2013, 2015), Delgado Mena et al. (2010), Adibekyan et al. (2012), Ramírez et al. (2012, 2013), Carretta et al. (2013), Mann et al. (2013a), Bensby et al. (2014), Battistini & Bensby (2015), da Silva et al. (2015), and Suárez-Andrés et al. (2017).

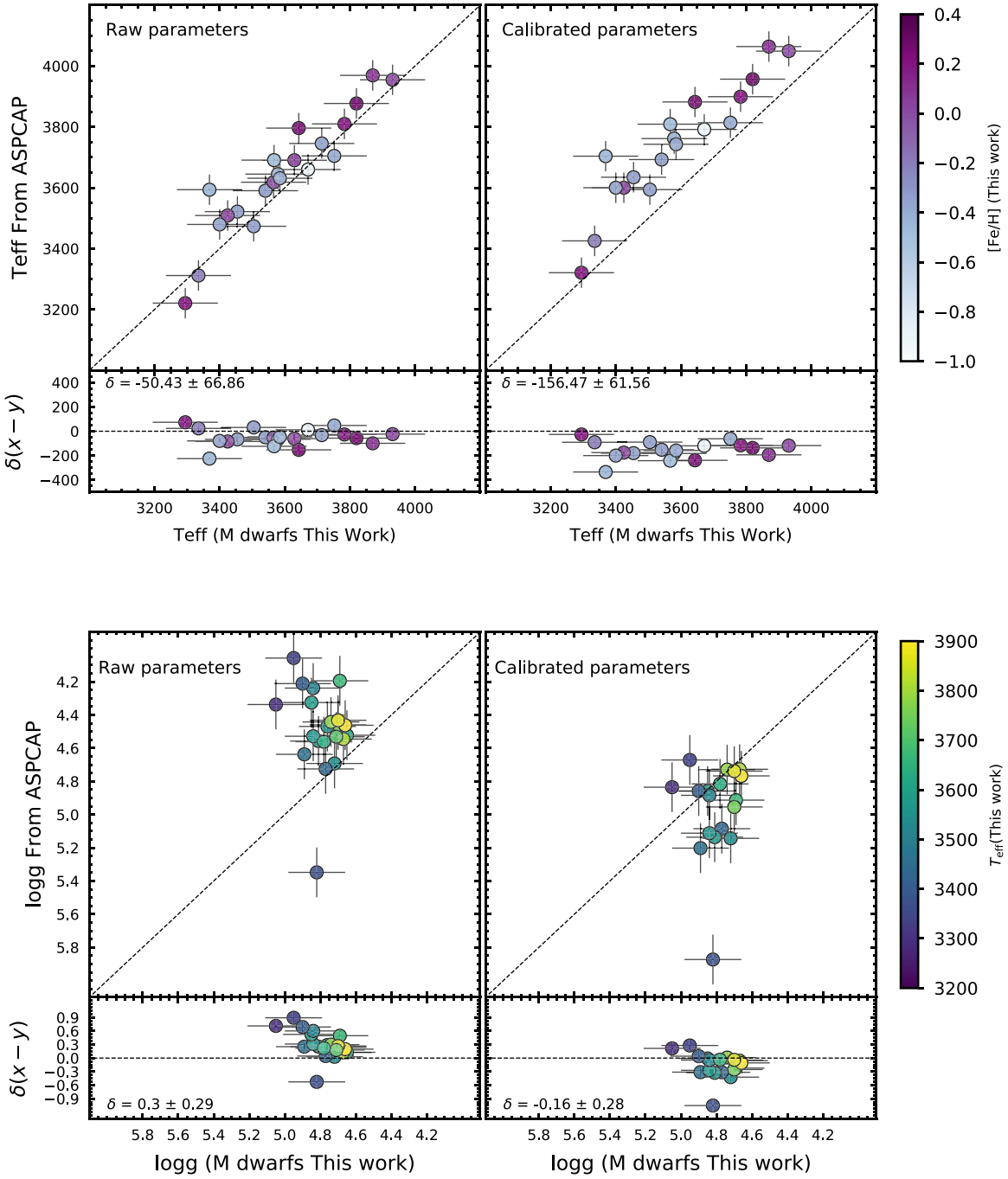

Figure 4. The $T_{\rm eff}$–$T_{\rm eff}$ (top panel) and the log g–log g (bottom panel) diagrams for this work and DR16 results, respectively. Left and right panels show the raw ASPCAP and the calibrated results from DR16. A residual diagram is presented at the bottom of each panel.

derived in DR16 is log $g = 5.35$ dex and δ log $g = -0.53$ dex. This star is the one in our sample with the highest rotational speed, with v sin $i = 13.5$ km s^{-1}. (The calibrated log g value for this star is log $g = 5.87$ dex, which is even more discrepant; see discussion below.)

It is known that ASPCAP has difficulties in determining good spectroscopic log g values; main-sequence FGK stars and red-giant stars present systematic offsets when compared to log g's from physical relations or from seismic results in the literature (e.g., Pinsonneault et al. 2014, 2018; Holtzman et al. 2018; Jönsson et al. 2018, 2020). Given the biased results for the APOGEE log g's, the APOGEE team calibrated the raw (spectroscopic) ASPCAP log g values and derived calibrated ones (shown in the bottom-right panel of Figure 4). For the calibrated log g values, there is an improvement in the comparison with our results; however, the raw ASPCAP log g values appear to have been overcorrected and the spread is still significant when compared to ours: $\langle \log g_{\rm this\ work} - \log g_{\rm DR16} \rangle = -0.16 \pm 0.28$ dex.

The comparison between the elemental abundances from DR16 with this work suggests that, taken as a whole, the ASPCAP abundances are lower than ours: $\langle [{\rm M/H}]_{\rm this\ work} - [{\rm M/H}]_{\rm DR16} \rangle = +0.21 \pm 0.07$ dex. The comparison for each studied element, along with the delta abundance difference for each element, are shown in Figure 5. The mean abundance differences for all elements are around ∼0.2 dex, with

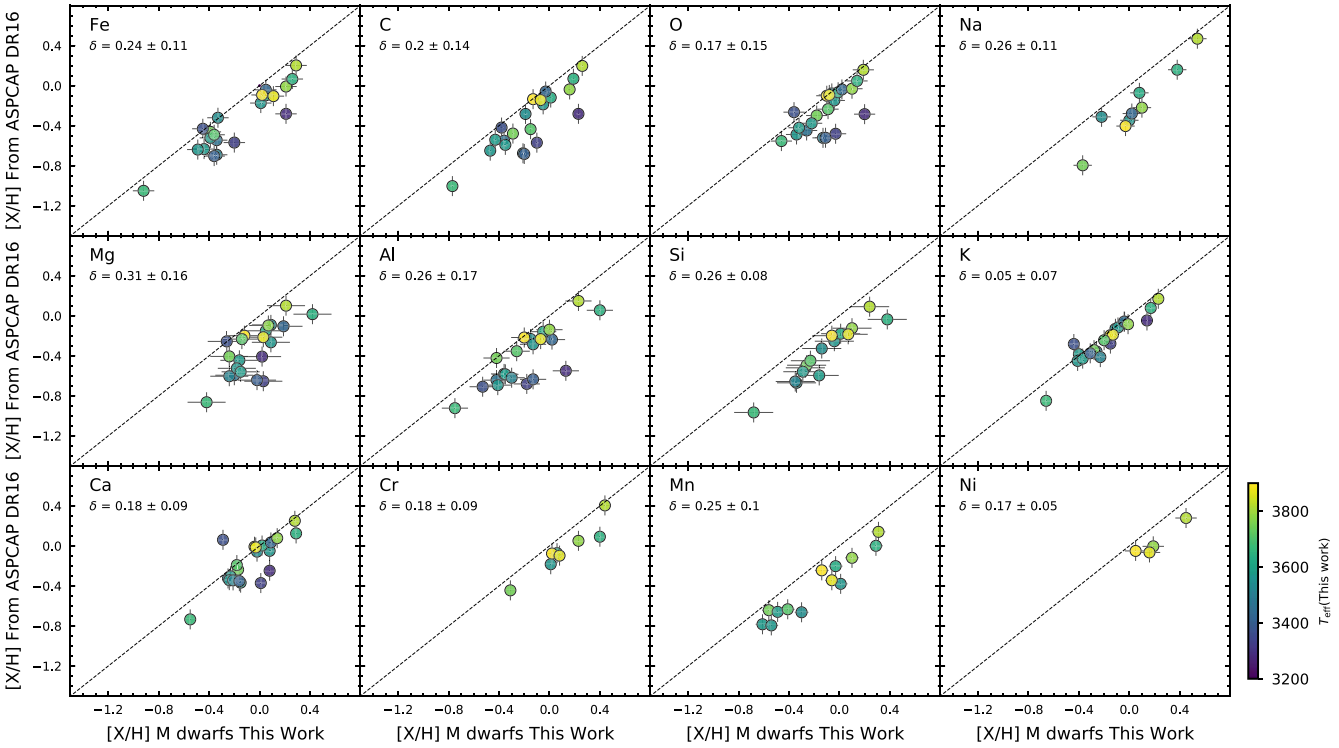

Figure 5. The [X/H]–[X/H] diagram with this work's M-dwarf abundances vs. the raw ASPCAP DR16 [X/H]. The delta abundance difference is given for each element in the panel.

exceptions being the K on one side ($\delta = 0.05 \pm 0.07$ dex) and Mg, for which the mean difference is larger and around 0.3 dex. There is a range in the values for the standard deviation of the mean. For Si and Mn, σ is $\leqslant 0.10$ dex, while the Mg and Al abundances display a higher and similar level of scatter ($\sigma = 0.17$ dex).

One element to discuss in particular is iron, as its abundance is typically used as an indicator of stellar metallicity. Abundances are often studied relative to metallicity and adopt the Sun as a reference, or use the [X/Fe] notation, where X represents the elemental abundance of each species. The derived iron abundances [X/H] are on average 0.24 dex higher than those from the DR16. (A similar abundance offset was also found in Souto et al. 2021, who analyzed a sample of M dwarfs belonging to the Coma Berenices open cluster.) In this context, we expect the [X/Fe] ratios between this work and DR16 to be more similar, as the offset is about ∼0.21 dex for most of the studied elements, removing some of the systematic differences when examining the variation with respect to the metallicity. A future effort using the methodology in this study will produce a revised set of improved results for all M dwarfs observed by APOGEE.

4.3. The Galactic Abundance Trends

The targeted M dwarfs are all within 100 pc and constitute a sample of low-mass stars in the solar neighborhood. The abundance results for 11 chemical elements for these M dwarfs offer the possibility, for the first time in the literature, to begin an investigation of chemical evolution trends via canonical diagrams of [X/Fe] versus [Fe/H] that include these low-mass M dwarfs—the dominant number population in the Galaxy. Such diagrams are presented in Figures 6 (for C, O, Mg, Si,and Ca) and 7 (for Na, Al, K, Cr, Mn, and Ni), where the abundance results for the M dwarfs are shown as red circles, with abundance uncertainties displayed for each star; results for the exoplanet-hosting M dwarfs Kepler 186, Kepler 138, and Ross 128 from our previous studies (Souto et al. 2017, 2018) are also displayed (red triangles). The [X/Fe] versus [Fe/H] trends for the M dwarfs shown in the different panels of Figures 6 and 7 are consistent with what is expected from Galactic chemical evolution and the behavior observed in field stars of spectral types FGK. Included in these figures are also comparisons with abundances from the literature.

Results for the [O/Fe], [C/Fe], [C/O], [Mg/Fe], [Si/Fe], and [Ca/Fe] ratios are shown in the different panels of Figure 6. The solid lines in the figure correspond to the running mean of 20 periods of the abundance results from the reference studies. Focusing first on oxygen, the various literature results delineate a trend that is expected from Galactic chemical evolution, as they map the decreasing [O/Fe] ratio as SN Ia begin to contribute with iron. We make no distinction between the low- and high-α sequences found for the Milky Way disk (Nidever et al. 2014). Overall, the behavior of [O/Fe] versus [Fe/H] is similar for all studies in the regime where they overlap in metallicity; our M-dwarf abundance ratios also follow a similar trend. A closer examination, however, reveals some systematic differences between the sets of results. It is apparent that our M-dwarf abundances are in better agreement with the median abundance relation from the results in Nissen et al. (2014; cyan squares), who studied carbon and oxygen abundances in a sample of FG main-sequence stars in the solar neighborhood from the C I line at λ5052.5 Å, and O I from both the triplet lines at λ7777 Å and the forbidden line at λ6300 Å. In addition, the M dwarf in our sample with the lowest metallicity ([Fe/H] ~ -0.90) has significantly enhanced in [O/Fe], as expected from the production of oxygen in SN II, and it follows the [O/Fe] distribution for metal-poor stars

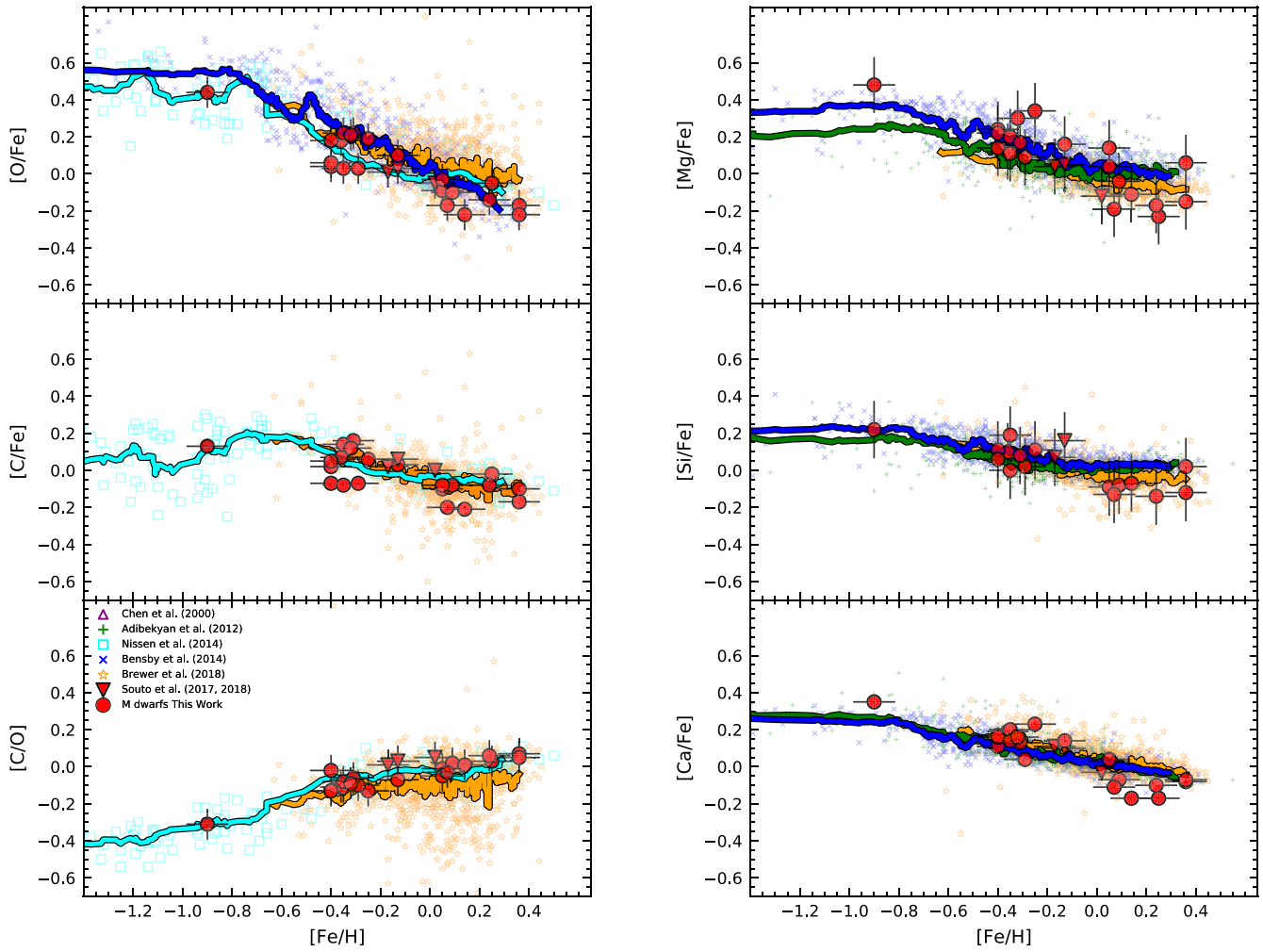

Figure 6. Left panel: the Galactic trends of [O, C, and C/O over Fe] as a function of [Fe/H] for the studied M dwarfs (red symbols). The Galactic field star results are from Nissen et al. (2014; cyan open squares), Bensby et al. (2014; blue Xs), and Brewer & Fischer (2018; orange stars). Right panel: the Galactic trends of the α elements [Mg, Si, and Ca/Fe] as a function of [Fe/H] for the studied M dwarfs (red symbols). The Galactic field star results are from Adibekyan et al. (2012; green pluses), Bensby et al. (2014; blue Xs), and Brewer & Fischer (2018; orange stars).

([Fe/H]<–0.8) in Nissen et al. (2014). Bensby et al. (2014) also analyzed the O I triplet lines at λ7777 Å in a sample of 714 F- and G-dwarf and subgiant stars. Our M-dwarf results lie roughly 0.10 dex below their median abundance curve (blue curve). The [O/Fe] versus [Fe/H] trend obtained from the large sample of FGK Kepler planet host stars in Brewer & Fischer (2018; orange curve) appear to be flatter compared to the other studies, including the results for the M dwarfs. There is also a clearly larger scatter in their oxygen abundance results (orange symbols), spreading from [O/Fe] ~ -0.40 up to $+0.90$ dex.

For carbon, there is a modest enhancement in [C/Fe] as [Fe/H] decreases; this ratio stays roughly constant for lower metallicities. Carbon is formed both in low-mass and high-mass stars. The results from all studies (this one included) agree quite well, without significant systematic differences. Again, the derived C abundances for the M dwarfs (red circles) agree with the FG dwarf results from Nissen et al. (2014). Our carbon results show slightly more scatter than theirs, but the match is nonetheless quite good (<0.10 dex across the [Fe/H] versus [O/Fe] diagram). The lowest metallicity M dwarf in our sample is also in line with [C/Fe] ratios for stars with similar metallicities, falling roughly in the median of the distribution of Nissen et al. (2014). The M dwarf [C/Fe] versus [Fe/H] results are also consistent with those from Brewer & Fischer (2018; orange symbols/curve), in this case also for FG stars, although there are several stars in their sample having significantly lower and higher values for [C/Fe] than ours.

Examining the [C/O] abundance ratio versus [Fe/H] diagram (bottom-left panel of Figure 6), reveals that the M-dwarf [C/O] ratios decrease with decreasing metallicity with a small scatter (~ -0.20–$+0.00$ dex), again showing excellent agreement with such ratios in Nissen et al. (2014).

Results for the α elements Mg, Si, and Ca are shown, respectively, in the top-right, middle, and bottom panels of Figure 6. The overall behavior of Mg/Fe, Si/Fe, and Ca/Fe with metallicity is similar to what is seen for oxygen-over-iron and what is expected from Galactic chemical evolution: the [Mg, Si, Ca /Fe] ratios exhibit an increase as [Fe/H] decreases, while a flat and enhanced [α/Fe], corresponding to early production in SN II, is reached near [Fe/H] ~ -1. An additional comparison for Mg, Si, and Ca in the Galactic disk was performed by Adibekyan et al. (2012), who analyzed a large sample of 1111 FGK dwarf stars from the High Accuracy Radial Velocity Planet Searcher program. The Mg, Si, and Ca abundances obtained here for the M dwarfs agree with the literature results, although our [Mg/Fe] ratios show more

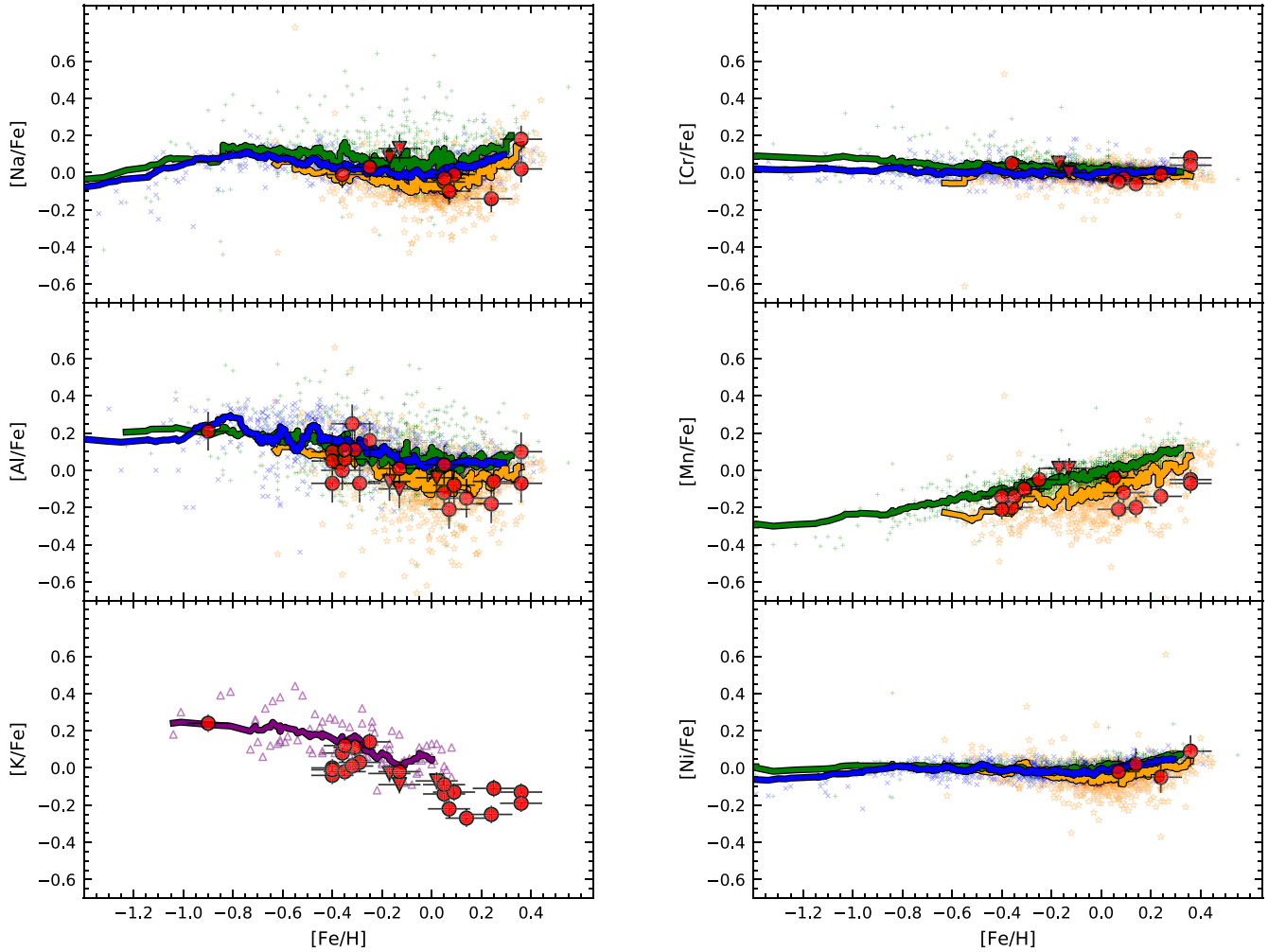

Figure 7. Left panel: the Galactic trends of [Na, Al, and K/Fe] as a function of [Fe/H] for the studied M dwarfs (red symbols). The Galactic field star results are from Adibekyan et al. (2012; green pluses), Bensby et al. (2014; blue Xs), Chen et al. (2000; purple triangles), and Brewer & Fischer (2018; orange stars). Right panel: the Galactic trends of the iron-peak elements [Cr, Mn, and Ni/Fe] as a function of [Fe/H] for the studied M dwarfs (red symbols). The Galactic field star results are from Adibekyan et al. (2012; green pluses), Bensby et al. (2014; blue Xs), and Brewer & Fischer (2018; orange stars).

scatter than the other studies. In addition, for metallicities solar and above, the M-dwarf [α/Fe] values are systematically lower than the literature Si and Ca abundances. Similar to what is found for oxygen, the [Mg/Fe], [Si/Fe], and [Ca/Fe] ratios in the lowest metallicity M dwarf studied are elevated: for Si there is good agreement with the median abundances from the sample in both Adibekyan et al. (2012) and Bensby et al. (2014), while we find a larger enhancement in [Mg/Fe] and [Ca/Fe] than in Adibekyan et al. (2012) and Bensby et al. (2014).

In the left panels of Figure 7, we present abundance results for the odd-Z elements: Na, Al, and K. There are many fewer M dwarfs with measurable Na abundances when compared to the other elements studied here, due to the fact that the Na I lines in the APOGEE M-dwarf spectra are weak and not measurable for all stars in the sample. The [Na/Fe] ratios obtained for the M dwarfs are within the Galactic range when considering the literature values shown in the figure, although some systematic differences between the studies are present. For both Na and Al the sequences defined by the median abundance values for the sample in each study are similar, but there are systematic differences, which are not surprising, at the level of 0.1–0.2 dex. The [Na/Fe] ratios from Bensby et al. (2014) overlap with the higher envelope in [Na/Fe] from Brewer & Fischer (2018), but the latter displays a lower sequence in [Na/Fe] that is not present in Bensby et al. (2014) that reduces the median abundance values. Adibekyan et al.'s (2012) [Na/Fe] ratios tend to scatter to higher values when compared to the other results. Our sodium abundances for the M dwarfs fall mostly along a low [Na/Fe] sequence and are in better agreement with the median values in Brewer & Fischer (2018); the Galactic trend of [Na/Fe] as a function of [Fe/H] displays the typical "peanut shape", with a clear upturn in [Na/Fe] for higher metallicities. The [Al/Fe] versus [Fe/H] abundance pattern obtained for the studied M dwarfs (Figure 7) is reminiscent of that of Na; here again our [Al/Fe] results are overall lower than Bensby et al. (2014) and Adibekyan et al. (2012) and are in better agreement with Brewer & Fischer (2018). Our results also show an upturn in [Al/Fe] for metallicities roughly above solar. For potassium there are fewer studies available in the literature, but we can compare our results for the M dwarfs with those from Chen et al. (2000). Their median [K/Fe] abundances rise as the metallicity decreases for metallicities solar and below (bottom-left panel of Figure 7). The [K/Fe] abundance ratios derived for the M dwarfs follow a similar sequence, but are offset by roughly −0.15 dex. At solar

metallicity, [Fe/H = 0], the [K/Fe] ratio for M dwarfs is also below solar by roughly 0.2 dex (although the Chen et al. 2000 sample do not populate this parameter space).

For the iron-peak elements Cr, Mn, and Ni (shown in the right panels of Figure 7), the derived M-dwarf abundances follow the same scale as Fe. The [Cr/Fe] and [Ni/Fe] ratios display similar behaviors, and there is good agreement between the results in all studies, including the Cr and Ni abundances for the M dwarfs derived here. (Ni abundances have not been derived for M dwarfs with metallicities roughly below solar because the Ni I spectral lines become too weak to be measurable, and there is only one reliably measurable Cr I line in the APOGEE spectra). The Mn results display an overall larger scatter when compared to Cr and Ni. There is a flat trend similar to those of Cr and Ni, although with a larger scatter. In fact, the Mn abundances derived in this work follow the trend of Mn abundances derived from non-LTE, as seen in Bergemann & Gehren (2008), for example, suggesting that non-LTE deviations are small for the lines in the APOGEE NIR spectra of mid-early M dwarf stars.

The recent work of Ishikawa et al. (2022) studied M-dwarf [X/Fe] ratios as a function of [Fe/H] for five species in common with this work. The overall trends of [Mg/Fe], [Cr/Fe], and [Mn/Fe] versus [Fe/H] in Ishikawa et al. (2022) are similar to the ones presented here, while their [Na/Fe] values versus [Fe/H] fall somwhat lower by ∼0.1 dex, and their [Ca/Fe] versus [Fe/H] trend is flatter.

5. Conclusions

M dwarfs are the most abundant stellar class in the Galaxy and yet their chemical content has just recently begun to be probed in detail. We report on abundances of the elements C, O, Na, Mg, Al, Si, K, Ca, Cr, Mn, Fe, and Ni measured in a sample of nearby field M dwarfs observed by the high-resolution NIR APOGEE survey. Our sample contains 11 M dwarf stars which are secondaries in wide binary systems, plus 10 M dwarfs with measured interferometric radii. The latter are benchmark comparisons for the effective temperatures, and, in principle, the wide binaries offer the possibility to probe if there are large and significant systematic differences between detailed chemical abundances of M dwarfs in comparison to the warmer primary stars analyzed from high-resolution optical spectra in the literature.

The use of warm primaries in binary systems as benchmark comparisons for M dwarfs makes the crucial assumption that the chemical compositions of the M dwarfs and the primary stars are the same. There may be some level of diffusion effects, which depend on the age and mass of the warm primaries; such effects reduce the original abundances by typically less than 0.10 dex, at most for turn-off stars and minimally for the M dwarfs. Diffusion effects can, however, be minimized by investigating abundance ratios, for example, relative to iron, as all chemical elements suffer from roughly similar levels of diffusion within a few hundredths of a decimal exponent (Choi et al. 2016). The comparison of the [C/Fe], [O/Fe], [Na/Fe], [Mg/Fe], [Al/Fe], [Si/Fe], [Ca/Fe], [Mn/Fe], and [Ni/Fe] abundance ratios for the M dwarfs and their warm primaries gives an offset of 0.01, −0.05, −0.05, 0.01, −0.08, −0.06, −0.08, 0.05, −0.04, respectively (with a mean abundance difference of -0.04 ± 0.04 dex). This indicates that the abundance scale for the M dwarfs in this study is precise, within the abundance uncertainties, and that the M-dwarf metallicities and detailed abundance distributions are close matches to their hotter primaries.

The chemical abundances of the M dwarfs were derived using a different methodology from that adopted by the APOGEE ASPCAP automatic abundance pipeline (García Pérez et al. 2016), although we used the same APOGEE updated line list (Smith et al. 2021). A comparison of our abundance results with those from ASPCAP DR16 indicates significant systematic offsets for all studied elements.

This sample of cool stars lies in the solar neighborhood, having distances within 100 pc, and represents one of the first samples of M dwarfs to have the abundances of 12 chemical elements along with chemical evolution trends investigated. Overall, the behavior of [X/Fe] versus [Fe/H] values, as shown in Figures 6 and 7, are within what is expected from Galactic chemical evolution, as well as in agreement with those observed for field FGK stars from the literature.

Beginning with carbon, there is a modest enhancement in [C/Fe] as [Fe/H] decreases, and this ratio stays roughly constant for lower metallicity stars; the [C/O] ratios decrease with decreasing metallicity with small scatter (∼−0.20–+0.00 dex). The results of [C/O], in particular, compare well with those of Nissen et al. (2014) and Brewer & Fischer (2018). The overall behavior of the α elements O, Mg, Si, and Ca with metallicity is in line with what is expected from Galactic chemical evolution. The [O/Fe], [Mg/Fe], [Si/Fe], and [Ca/Fe] ratios rise as the metallicity declines, while the lowest metallicity M dwarfs have enhanced α/Fe: Si and Ca measurements display good agreement with the median abundances from Adibekyan et al. (2012) and Bensby et al. (2014), while for Mg there is also good agreement though our results show more scatter.

The abundance trends obtained for odd-Z elements Na and Al obtained for the M dwarfs are within the range of the literature values. At solar metallicities and above the M dwarfs exhibit the same trend of increasing Na/Fe and Al/Fe values as found for the FGK stars. The [K/Fe] abundances rise as the metallicity decreases for metallicities solar and below. For the iron-peak elements Cr, Mn, and Ni, the derived M-dwarf abundances overall track that of iron closely. The Mn abundances derived follow the trend from the non-LTE calculations from Bergemann & Gehren (2008), suggesting that non-LTE deviations are small for the Mn I lines in the APOGEE spectra of mid-early M dwarf stars.

The methodology in this work and previous works of our team (Souto et al. 2020, 2021) will be the basis for the reanalysis of all M dwarfs observed by APOGEE in future work. Also, the chemical abundances for the three exoplanet-hosting M dwarfs in our sample can be used to study the planet–star connections and interior structures of those exoplanets.

K.C. and V.S. acknowledge that their work here is supported, in part, by the National Science Foundation through NSF grant No. AST-2009507, as well as by the National Aeronautics and Space Administration under grant No. 16-XRP16_2-0004, issued through the Astrophysics Division of the Science Mission Directorate. D.A.G.H., O.Z., and T.M. acknowledge support from the State Research Agency (AEI) of the Ministry of Science, Innovation and Universities (MCIU) and the European Regional Development Fund (FEDER) under grant No. AYA2017-88254-P. S.M. acknowledges the Penn State's Center for Exoplanets and

Habitable worlds. B.R.-A. acknowledges funding support from FONDECYT through grant No. 11181295.

Funding for the Sloan Digital Sky Survey-IV has been provided by the Alfred P. Sloan Foundation, the U.S. Department of Energy Office of Science, and the Participating Institutions. SDSS-IV acknowledges support and resources from the Center for High-Performance Computing at the University of Utah. The SDSS website is www.sdss.org.

SDSS-IV is managed by the Astrophysical Research consortium for the Participating Institutions of the SDSS Collaboration including the Brazilian Participation Group, the Carnegie Institution for Science, Carnegie Mellon University, the Chilean Participation Group, the French Participation Group, Harvard-Smithsonian Center for Astrophysics, Instituto de Astrofísica de Canarias, The Johns Hopkins University, Kavli Institute for the Physics and Mathematics of the Universe (IPMU)/University of Tokyo, Lawrence Berkeley National Laboratory, Leibniz Institut für Astrophysik Potsdam (AIP), Max-Planck-Institut für Astronomie (MPIA Heidelberg), Max-Planck-Institut für Astrophysik (MPA Garching), Max-Planck-Institut für Extraterrestrische Physik (MPE), National Astronomical Observatory of China, New Mexico State University, New York University, University of Notre Dame, Observatório Nacional/MCTI, The Ohio State University, Pennsylvania State University, Shanghai Astronomical Observatory, United Kingdom Participation Group, Universidad Nacional Autónoma de México, University of Arizona, University of Colorado Boulder, University of Oxford, University of Portsmouth, University of Utah, University of Virginia, University of Washington, University of Wisconsin, Vanderbilt University, and Yale University.

Facility: Sloan.

Software: Turbospectrum (Alvarez & Plez 1998, Plez 2012), MARCS (Gustafsson et al. 2008), Bacchus (Masseron et al. 2016), Matplotlib (Hunter 2007), Numpy (van der Walt et al. 2011).

ORCID iDs

Diogo Souto https://orcid.org/0000-0002-7883-5425
Katia Cunha https://orcid.org/0000-0001-6476-0576
Verne V. Smith https://orcid.org/0000-0002-0134-2024
C. Allende Prieto https://orcid.org/0000-0002-0084-572X
Kevin Covey https://orcid.org/0000-0001-6914-7797
D. A. García-Hernández https://orcid.org/0000-0002-1693-2721
Jon A. Holtzman https://orcid.org/0000-0002-9771-9622
Henrik Jönsson https://orcid.org/0000-0002-4912-8609
Suvrath Mahadevan https://orcid.org/0000-0001-9596-7983
Steven R. Majewski https://orcid.org/0000-0003-2025-3147
Thomas Masseron https://orcid.org/0000-0002-6939-0831
Marc Pinsonneault https://orcid.org/0000-0002-7549-7766
Donald P. Schneider https://orcid.org/0000-0001-7240-7449
Keivan G. Stassun https://orcid.org/0000-0002-3481-9052
Ryan Terrien https://orcid.org/0000-0002-4788-8858
Olga Zamora https://orcid.org/0000-0003-2100-1638
Guy S. Stringfellow https://orcid.org/0000-0003-1479-3059
Richard R. Lane https://orcid.org/0000-0003-1805-0316
Christian Nitschelm https://orcid.org/0000-0003-4752-4365
Bárbara Rojas-Ayala https://orcid.org/0000-0002-0149-1302

References

Abolfathi, B., Aguado, D. S., Aguilar, G., et al. 2018, ApJS, 235, 42
Adibekyan, V. Z., Sousa, S. G., Santos, N. C., et al. 2012, A&A, 545, A32
Ahn, C. P., Alexandroff, R., Allende Prieto, C., et al. 2014, ApJS, 211, 17
Ahumada, R., Prieto, C. A., Almeida, A., et al. 2020, ApJS, 249, 3
Alam, S., Albareti, F. D., Allende Prieto, C., et al. 2015, ApJS, 219, 12
Allard, F., Hauschildt, P. H., & Schwenke, D. 2000, ApJ, 540, 1005
Alvarez, R., & Plez, B. 1998, A&A, 330, 1109
Barber, R. J., Tennyson, J., Harris, G. J., et al. 2006, MNRAS, 368, 1087
Battistini, C., & Bensby, T. 2015, A&A, 577, A9
Bean, J. L., Sneden, C., Hauschildt, P. H., et al. 2006, ApJ, 652, 1604
Bensby, T., Feltzing, S., & Oey, M. S. 2014, A&A, 562, A71
Bergemann, M., & Gehren, T. 2008, A&A, 492, 823
Bertelli Motta, C., Pasquali, A., Richer, J., et al. 2018, MNRAS, 478, 425
Birky, J., Hogg, D. W., Mann, A. W., et al. 2020, ApJ, 892, 31
Blanton, M. R., Bershady, M. A., Abolfathi, B., et al. 2017, AJ, 154, 28
Bonfils, X., Delfosse, X., Udry, S., et al. 2005, A&A, 442, 635
Boyajian, T. S., von Braun, K., van Belle, G., et al. 2012, ApJ, 757, 112
Brewer, J. M., & Fischer, D. A. 2018, ApJS, 237, 38
Carretta, E., Gratton, R. G., Bragaglia, A., et al. 2013, ApJ, 769, 40
Chavez, J., & Lambert, D. L. 2009, ApJ, 699, 1906
Chen, Y. Q., Nissen, P. E., Zhao, G., et al. 2000, A&AS, 141, 491
Choi, J., Dotter, A., Conroy, C., et al. 2016, ApJ, 823, 102
Covey, K. R., Lada, C. J., Román-Zúñiga, C., et al. 2010, ApJ, 722, 971
da Silva, R., Milone, A. de, C., & Rocha-Pinto, H. J. 2015, A&A, 580, A24
Delgado Mena, E., Israelian, G., González Hernández, J. I., et al. 2010, ApJ, 725, 2349
Dotter, A., Conroy, C., Cargile, P., & Asplund, M. 2017, ApJ, 840, 99
Gao, X., Lind, K., Amarsi, A. M., et al. 2018, MNRAS, 481, 2666
García Pérez, A. E., Allende Prieto, C., Holtzman, J. A., et al. 2016, AJ, 151, 144
González-Álvarez, E., Zapatero Osorio, M. R., Caballero, J. A., et al. 2020, A&A, 637, A93
Gunn, J. E., Siegmund, W. A., Mannery, E. J., et al. 2006, AJ, 131, 2332
Gustafsson, B., Edvardsson, B., Eriksson, K., et al. 2008, A&A, 486, 951
Hargreaves, R. J., Hinkle, K. H., Bauschlicher, C. W., et al. 2010, AJ, 140, 919
Henry, T. J., Jao, W.-C., Winters, J. G., et al. 2018, AJ, 155, 265
Hinkel, N. R., Timmes, F. X., Young, P. A., et al. 2014, AJ, 148, 54
Holtzman, J. A., Hasselquist, S., Shetrone, M., et al. 2018, AJ, 156, 125
Hunter, J. D. 2007, CSE, 9, 90
Ishikawa, H. T., Aoki, W., Hirano, T., et al. 2022, AJ, 163, 72
Ishikawa, H. T., Aoki, W., Kotani, T., et al. 2020, PASJ, 72, 102
Jönsson, H., Allende Prieto, C., Holtzman, J. A., et al. 2018, AJ, 156, 126
Jönsson, H., Holtzman, J. A., Allende Prieto, C., et al. 2020, AJ, 160, 120
Lindgren, S., & Heiter, U. 2017, A&A, 604, A97
Lindgren, S., Heiter, U., & Seifahrt, A. 2016, A&A, 586, A100
Mahadevan, S., Ramsey, L., Bender, C., et al. 2012, Proc. SPIE, 8446, 84461S
Majewski, S. R., Schiavon, R. P., Frinchaboy, P. M., et al. 2017, AJ, 154, 94
Mann, A. W., Brewer, J. M., Gaidos, E., et al. 2013a, AJ, 145, 52
Mann, A. W., Gaidos, E., & Ansdell, M. 2013b, ApJ, 779, 188
Masseron, T., Merle, T., & Hawkins, K. 2016, BACCHUS: Brussels Automatic Code for Characterizing High accUracy Spectra, Astrophysics Source Code Library ascl:1605.004
Michaud, G., Alecian, G., & Richer, J. 2015, Atomic Diffusion in Stars, Astronomy and Astrophysics Library (Cham: Springer)
Miller, G. E., & Scalo, J. M. 1979, ApJS, 41, 513
Mishenina, T., Gorbaneva, T., Pignatari, M., et al. 2015, MNRAS, 454, 1585
Mishenina, T. V., Pignatari, M., Korotin, S. A., et al. 2013, A&A, 552, A128
Mishenina, T. V., Soubiran, C., Bienaymé, O., et al. 2008, A&A, 489, 923
Montes, D., González-Peinado, R., Tabernero, H. M., et al. 2018, MNRAS, 479, 1332
Newton, E. R., Charbonneau, D., Irwin, J., et al. 2014, AJ, 147, 20
Nidever, D. L., Bovy, J., Bird, J. C., et al. 2014, ApJ, 796, 38
Nidever, D. L., Holtzman, J. A., Allende Prieto, C., et al. 2015, AJ, 150, 173
Nissen, P. E., Chen, Y. Q., Carigi, L., et al. 2014, A&A, 568, A25
Passegger, V. M., Reiners, A., Jeffers, S. V., et al. 2018, A&A, 615, A6
Pinamonti, M., Damasso, M., Marzari, F., et al. 2018, A&A, 617, A104
Pinsonneault, M. H., Elsworth, Y., Epstein, C., et al. 2014, ApJS, 215, 19
Pinsonneault, M. H., Elsworth, Y. P., Tayar, J., et al. 2018, ApJS, 239, 32
Pinsonneault, M. H., Kawaler, S. D., Sofia, S., et al. 1989, ApJ, 338, 424
Plez, B. 2012, Turbospectrum: Code for spectral synthesis1205, Astrophysics Source Code Library ascl:1205.004
Quirrenbach, A., Amado, P. J., Caballero, J. A., et al. 2014, Proc. SPIE, 9147, 91471F
Rajpurohit, A. S., Allard, F., Teixeira, G. D. C., et al. 2018, A&A, 610, A19
Ramírez, I., Allende Prieto, C., & Lambert, D. L. 2013, ApJ, 764, 78
Ramírez, I., Fish, J. R., Lambert, D. L., et al. 2012, ApJ, 756, 46
Reddy, B. E., Lambert, D. L., & Allende Prieto, C. 2006, MNRAS, 367, 1329
Reiners, A., Zechmeister, M., Caballero, J. A., et al. 2018, A&A, 612, A49
Rojas-Ayala, B., Covey, K. R., Muirhead, P. S., et al. 2010, ApJL, 720, L113

Rojas-Ayala, B., Covey, K. R., Muirhead, P. S., et al. 2012, ApJ, 748, 93
Sarmento, P., Rojas-Ayala, B., Delgado Mena, E., et al. 2021, A&A, 649, A147
Semenova, E., Bergemann, M., Deal, M., et al. 2020, A&A, 643, A164
Shetrone, M., Bizyaev, D., Lawler, J. E., et al. 2015, ApJS, 221, 24
Shi, J. R., Gehren, T., & Zhao, G. 2004, A&A, 423, 683
Smith, V. V., Bizyaev, D., Cunha, K., et al. 2021, AJ, 161, 254
Soubiran, C., & Girard, P. 2005, A&A, 438, 139
Souto, D., Allende Prieto, C., Cunha, K., et al. 2019, ApJ, 874, 97
Souto, D., Cunha, K., García-Hernández, D. A., et al. 2017, ApJ, 835, 239
Souto, D., Cunha, K., Smith, V. V., et al. 2018, ApJ, 857, 14
Souto, D., Cunha, K., Smith, V. V., et al. 2020, ApJ, 890, 133
Souto, D., Cunha, K., & Smith, V. V. 2021, ApJ, 917, 11
Souto, D., Unterborn, C. T., Smith, V. V., et al. 2018, ApJL, 860, L15
Stock, S., Nagel, E., Kemmer, J., et al. 2020, A&A, 643, A112
Suárez-Andrés, L., Israelian, G., González Hernández, J. I., et al. 2017, A&A, 599, A96
Terrien, R. C., Mahadevan, S., Deshpande, R., et al. 2015, ApJS, 220, 16
Tsuji, T., & Nakajima, T. 2014, PASJ, 66, 98
Tsuji, T., & Nakajima, T. 2016, PASJ, 68, 13
Tsuji, T., Nakajima, T., & Takeda, Y. 2015, PASJ, 67, 26
van der Walt, S., Colbert, S. C., & Varoquaux, G. 2011, CSE, 13, 22
Veyette, M. J., Muirhead, P. S., Mann, A. W., et al. 2017, ApJ, 851, 26
Wilson, J. C., Hearty, F. R., Skrutskie, M. F., et al. 2019, PASP, 131, 055001
Woolf, V. M., & Wallerstein, G. 2005, MNRAS, 356, 963
Woolf, V. M., & Wallerstein, G. 2020, MNRAS, 494, 2718
Zamora, O., Garcı´a-Hernández, D. A., Allende, C., et al. 2015, AJ, 149, 181